Applied Surface Science 563 (2021) 150360

Contents lists available at ScienceDirect

Applied Surface Science

journal homepage: www.elsevier.com/locate/apsusc

Full Length Article

Solvothermal growth of {0 0 1} exposed anatase nanosheets and their ability to mineralize organic pollutants. The effect of alcohol type and content on the nucleation and growth of TiO_2 nanostructures

Szymon Dudziak [a], Marta Kowalkińska [a], Jakub Karczewski [c], Marcin Pisarek [d], Katarzyna Siuzdak [e], Adam Kubiak [f], Katarzyna Siwińska-Ciesielczyk [f], Anna Zielińska-Jurek [a,b,*]

[a] Department of Process Engineering and Chemical Technology, Faculty of Chemistry, Gdańsk University of Technology, G. Narutowicza 11/12, 80-233 Gdansk, Poland
[b] EcoTech Center, Gdańsk University of Technology, G. Narutowicza 11/12, 80-233 Gdańsk, Poland
[c] Institute of Nanotechnology and Materials Engineering, Faculty of Applied Physics and Mathematics, Gdańsk University of Technology, G. Narutowicza 11/12, 80-233 Gdańsk, Poland
[d] Institute of Physical Chemistry, Polish Academy of Sciences, Kasprzaka 44/52, 01−224 Warsaw, Poland
[e] Centre for Plasma and Laser Engineering, The Szewalski Institute of Fluid-Flow Machinery Polish Academy of Sciences, Fiszera 14, 80-231 Gdańsk, Poland
[f] Institute of Chemical Technology and Engineering, Faculty of Chemical Technology, Poznań University of Technology, Berdychowo 4, 60-965 Poznań, Poland

ARTICLE INFO

Keywords:
2D TiO_2 nanosheets
Photocatalysis
Crystal facet engineering
Phenol degradation
Mineralization efficiency

ABSTRACT

Herein, the series of {0 0 1} exposed anatase nanosheets from HF-assisted solvothermal growth synthesis were obtained. The two-dimensional TiO_2 were characterized, including both bulk (XRD, DR-UV–Vis, Mott-Schottky) and surface characteristics (N_2 sorption, XPS, SEM) with experimental results compiled with Density Functional Theory (DFT) calculations. The effect of alcohol amount and type was studied, demonstrating the crucial role of nucleation rate on the final material properties, which was connected with the possible ligand exchange between F^- and ROH in the $[TiF_6]^{2-}$ octahedra, leading to further TiO_2 condensation through an ether elimination reaction. Highly active 2D nanoparticles were easily obtained for different reaction times when a moderate amount of n-butanol or n-hexanol was introduced to the synthesis. The photoactivity of 2D TiO_2 with exposed {0 0 1} facet strongly depended on the photocatalytic available surface area with an increased amount of *ortho*–hydroxyphenol (catechol) formed as a by-product. Meanwhile, the rise of n-butanol or n-hexanol content during solvothermal reaction or changing it to ethanol allowed to form smaller and more crystalline anatase particles, but their activity was hindered. For these samples, the slow phenol disappearance and no catechol formation occurred due to (i) a lower amount of adsorbed fluorine, (ii) band position shifting towards lower values, and (iii) the surface presence of Ti^{3+}, which prevented the generation of $^{\bullet}OH$ radicals. It was also found that changing the nucleation rate by modifying the reaction environment influences the fluorine ions distribution, determining the final properties of 2D structure photocatalyst.

1. Introduction

Over the past years, photocatalytic degradation of persistent organic pollutants became one of the most studied technological issues. In photocatalytic reaction, the ability to generate reactive oxygen species or induce charge transfer directly to a contaminant during irradiation has been examined extensively for various materials [1–3]. Within them, TiO_2 is presented as one of the most chemically stable photocatalysts, with much attention being given to describe the mechanism responsible for its photocatalytic activity in both pure and modified form [4].

The correlation between morphological properties of semiconductor materials and their photocatalytic activity is crucial for design new and more efficient photocatalytic systems. The possibility of using the knowledge of crystallography of single crystals in the research of nanocrystals with facet exposition is a key to understand crystal growth and surface chemistry at nanoscale. In this regard, understanding the formation of anatase materials with exposed specific crystal facets

* Corresponding author at: Department of Process Engineering and Chemical Technology, Faculty of Chemistry, Gdańsk University of Technology, G. Narutowicza 11/12, 80-233 Gdansk, Poland.
E-mail address: annjurek@pg.edu.pl (A. Zielińska-Jurek).

https://doi.org/10.1016/j.apsusc.2021.150360
Received 15 January 2021; Received in revised form 24 May 2021; Accepted 9 June 2021
Available online 11 June 2021

allows studying their interactions with chemical species at the atomic level and may contribute to the improved photocatalytic activity. The surface energy of {001} facets is significantly higher than other low-index crystal planes (0.90 $J \cdot m^{-2}$). Therefore, they are not supposed to be exposed in anatase nanocrystals [5]. Initially, such particles' crystal growth was confined within the kinetically controlled regime under nonequilibrium conditions, e.g., the gas-phase thermal oxidation of $TiCl_4$ at high temperature or rapid heating and quenching of $Ti(OC_4H_9)_4$ [6]. However, Yang et al. have shown that fluorine ions can stabilize the {001} structure, promoting its exposition instead of the thermodynamically favored {1 0 1} facet [7]. The {001} facet of TiO_2 particles is described as more active than TiO_2 enclosed by other facets [7–8]. Notably, a positive influence of the {001} facet exposition on acetaldehyde, coumarin, methyl orange, and terephthalic acid photodegradation was reported, however, without considering their detailed study of transformation products formation and mineralization [9–12]. In this regard, some aspects of the photocatalytic activity of {001} exposed particles require further investigation.

In this regard, the photocatalytic activity and mineralization ability of the 2D structure anatase with exposed {001} facet was investigated using phenol as a model pollutant. Phenol and its derivatives are the commonly encountered organic contaminants in industrial effluents that have caused severe environmental problems [13]. Phenolic compounds are persistent and have acute toxicity with carcinogenic and mutagenic character. The US Environmental Protection Agency (EPA) and the European Union (EU) have classified phenolic compounds as priority pollutants since they are harmful to organisms even at low concentrations. The discharge limits of phenols in surface water must not exceed a concentration of 1 $mg \cdot dm^{-3}$.

Therefore, phenol removal from wastewater using heterogeneous photocatalysis is intensively studied. The mechanism of phenol photocatalytic degradation proceeds by the attack of photogenerated radicals on the benzene ring [14–18]. The created phenoxy radical initiates further transformations to form dihydroxylated products, such as commonly reported *ortho*-hydroxyphenol (catechol) and *para*-hydroxyphenol (hydroquinone). Further oxidation of these compounds leads to (i) formation of more hydroxylated intermediate products, (ii) opening of the phenyl ring and the formation of short aliphatic compounds, and (iv) final mineralization to carbon(IV) oxide and water [19–20].

Furthermore, a clear identification of different intermediates and photodegradation pathways of phenol degradation is essential because some of the by-products formed, e.g., hydroquinone and benzoquinone, are much more toxic than phenol itself. Therefore, the oxidation route of phenol has been the subject of studies in the last two decades. The mechanism of phenol degradation is strictly dependent on photodegradation reaction parameters, including solution pH, photocatalyst loading and type, ionic composition of wastewater, oxidant concentration, as well as light intensity and range [21–24]. Krivec et al. studied the effect of different process parameters, including residence time, initial phenol concentration, pH value, and UV light irradiation intensity on phenol photodegradation in a microreactor with a TiO_2 layer immobilized on the reactor inner walls [25]. They reported that selective oxidation of phenol to catechol proceeds very slow and that the generation of benzoquinone was completely suppressed. The total organic carbon analysis showed that phenol mineralization did not occur at any of the performed experimental conditions, possibly due to the strong adsorption of intermediates during laminar flow conditions in the microreactor. The reaction pathway of phenol degradation, involving only hydroquinone as the reaction intermediate, was probably related to anatase crystallite size [25].

Emeline et al. reported that the surface active sites responsible for the formation of catechol were less active in phenol photodegradation over six commercial TiO_2 samples (Degussa P-25, Hombikat UV100, ST-41, ST-21, FTL-200), which differed in polymorphic phase composition, crystallite size, and surface area. Simultaneously, within the series of analyzed TiO_2 samples, a positive correlation between selectivity and photocatalytic activity was observed for hydroquinone produced by both oxidation and reduction pathways [26]. On the contrary, Suhadolnik et al. reported that most of the phenol was converted to benzoquinone during photodegradation in TiO_2-nanotubes-based, coil-type photo-electrocatalytic microreactor [27]. Phenol degradation and mineralization were inefficient due to the increased electron-hole recombination. The complete degradation and mineralization were observed only after applying electrical potential [27]. Wang et al. have shown that crystallites/nanoparticles size is crucial to achieving high photocatalytic activities [28]. Moreover, it is known that different photocatalyst types could result in a degradation pathway to different intermediates [29], which might affect on mineralization degree [25].

Furthermore, it is also expected that the photocatalyst morphology should affect a phenol photocatalytic degradation mechanism [30]. The observed correlations between the activity and selectivity of TiO_2 photocatalysts toward primary phenol by-products can result from the difference in surface concentration of charge carriers and corresponding surface active sites, which might depend on the types of dominating surface faces [26–31]. Therefore, the role of the surface structure of photocatalyst is crucial in the photodegradation processes. Gao et al. observed that phenol removal is a facet-dependent process concerning Pt-modified TiO_2; however, only microcrystals with a single morphology were studied [32]. Also, in the previous work, we have reported that {1 0 1} exposed particles are suitable for the mineralization of phenol under UV–Vis irradiation, and the efficiency declines with the rise of {001} facets content in decahedral nanostructures [33]. However, due to the limited exposition of the {001} surface (up to ~ 17%) and relatively small sample set, the in-depth analysis with respect to the surface structure and other physicochemical features, such as nanoparticles size, was severely straitened during this work [33]. Therefore, there is still a lack of detailed information about the correlation between the individual exposed facet, size of the nanoparticles, their crystallinity, and composition on the photocatalytic degradation of organic pollutants, including phenol.

Therefore, the ability of the 2D structured anatase with a majority of exposed highly energetic {001} facets to mineralize organic pollutants was studied in detail. To best understand their influence on the photocatalytic process, series of {001} exposed TiO_2 nanoparticles differing in their physicochemical parameters have been prepared. The preparation procedure included TiO_2 hydrolysis from the titanium *tert*-butoxide in the presence of HF and different alcohols as additional reagents. This allowed us to obtain anatase particles with (i) high {001} facet exposition, (ii) different size, (iii) shape and (iv) crystallinity. Yang et al. have emphasized that the addition of aliphatic alcohol can strengthen the stabilization effect associated with fluorine adsorption over (001) surface and thus stimulate its preferred growth [34]. However, outside of this, information about the exact alcohol role in the crystallization process is rather limited. Therefore, we have discussed our results to give more detailed insight into alcohol's role in this synthesis procedure and how it helps to achieve different morphological features of the 2D anatase nanoparticles. Additionally, to better understand the obtained samples' morphological properties, the electronic structure of anatase and its {001} surface slab models were investigated computationally using density functional theory calculations.

2. Experimental section

The synthesis of 2D structure titanium(IV) oxide nanosheets was carried out by a facile solvothermal method. Tetrabutyltitanate (TBT), n-hexanol, n-butanol, ethanol, methanol, and hydrofluoric acid (48%) were used as received from Sigma-Aldrich without further purification.

2.1. Fabrication of TiO_2 nanosheets

During a typical preparation of 2D TiO_2, 17 cm^3 of TBT was introduced to the 200 cm^3 Teflon-lined stainless-steel reactor, together with

3.4 cm^3 of HF solution (48%) and was kept at 210 °C for various times to observe the growth of the nanocrystals (mentioned times include heating of the oven from room temperature to 210 °C, which takes approximately 1.5 h). Moreover, to achieve the highest possible control over the reaction, the addition of n-hexanol, n-butanol, ethanol, and methanol as solvents was investigated in different amounts: 10 cm^3, 30 cm^3, or 60 cm^3 of alcohol. After each reaction, nanoparticles were centrifuged and washed several times with ethanol, followed by water to remove residual organic species and ions. During the second part of the washing, 0.1 M solution of NaOH was introduced once per sample to help remove adsorbed fluorine ions. Separated nanosheets were then dried at 80 °C to gain the final material.

Obtained samples are denoted as SolventX-Yh, where X is the solvent volume (Me stands for methanol, Et for ethanol, But for n-butanol and Hex for n-hexanol), and Y is the reaction time. For example, But30-8h is an as-synthesized photocatalyst for which 30 cm^3 of n-butanol was used during the 8 h of the solvothermal process.

2.2. Material characterization

The samples and phase composition structure were investigated by X-ray powder diffraction (Cu Kα radiation, Rigaku MiniFlex 600 X-Ray diffractometer). The analyses and Rietveld refinements were performed with the HighScorePlus software package (PANalytical, 2006) and the ICDD database with data fitting based on the pseudo-Voigt profile function. The specimen displacement, lattice parameters, polynomial coefficients for the background function, profile parameters, and Gaussian and Lorentzian profile coefficients were refined. To determine the possible amorphous phase content in the samples, XRD analyses were carried out with crystalline NiO as an internal standard [35].

The nanostructures' morphology was characterized by field emission scanning electron microscopy (SEM, FEI Quanta FEG 250). Before the observations, all samples were coated with an Au layer to help discharge the excess electrons during the analysis. The observed particles' size was measured in two dimensions for the selected samples, and the obtained datasets were fitted with log-normal functions to obtain size probability distributions. The fitting details are presented in Supplementary Materials (Section 1), and the results were used to analyze the facet exposition observed under SEM.

An ASAP 2020 physisorption analyzer (Micromeritics Instrument Co., USA) was used to determine the surface parameters of the obtained nanoparticles, including Brunauer–Emmett–Teller (BET) surface area pore volume and pore size using low-temperature N_2 sorption. Before measurement, the analyzed materials were degassed at 120 °C for 4 h. The surface area was determined by the multipoint BET method using adsorption data for relative pressure (p/p_0) in the range 0.05–0.30.

A Microlab 350 (Thermo Electron) XPS spectrometer with non-monochromatic Al Kα radiation (hν = 1486.6 eV, power 300 W, voltage 15 kV) was used to determine the surface chemistry of the received materials. The analyzed area was 2x5 mm. The hemispherical analyzer was used for collecting the high-resolution (HR) XPS spectra with the following parameters: pass energy 40 eV, energy step size 0.1 eV. The collected XPS spectra were fitted using the Avantage software (version 5.9911, Thermo Fisher Scientific), where a Smart function of background subtraction was used to obtain XPS signal intensity, and an asymmetric Gaussian/Lorentzian mixed-function was applied. The carbon C1s peak position was assumed to be at 285.0 eV and used as an internal standard to determine other photoelectron peaks' binding energy.

The optical properties were studied in the range from 190 nm to 1100 nm (6.53 – 1.13 eV) by a UV–Vis spectrophotometer (Thermo Fisher Scientific Evolution 220) for the measurement of diffuse reflectance (DRS), using $BaSO_4$ as a standard.

2.3. Computational details

The electronic structure of bulk anatase and its (0 0 1) surface slab models were investigated computationally using density functional theory calculations within the generalized gradient approximation, as implemented in Quantum Espresso 6.5 software package [36,37]. All calculations were performed using ultrasoft pseudopotentials with Perdew-Burke-Ernzerhof (PBE [38]) exchange-corrected functionals, and the electronic wave functions were expanded to the energy cut-off of 500 eV. During the bulk calculations, the 2 × 1 × 1 anatase supercell was used, while for the (0 0 1) surface, the 2 × 1 slab with 3-titanium layers along the *l* direction was created, separated by a 20 Å layer of vacuum. K-point grids of 4 × 5 × 3 and 5 × 5 × 1 were used for the bulk and slab models, respectively. Next to the pure structures, oxygen vacancy and fluorine doping were modeled by removing a single O atom, replacing an O atom with F, and inserting F atoms at the interstitial position. Before the final calculations, all structures were allowed to relax using Broyden–Fletcher–Goldfarb–Shanno method with the threshold of 10^{-3} $Ry \cdot Bohr^{-1}$. In the (0 0 1) slab, one of the outermost Ti—O layers was kept fixed during the optimization. Optimized structures are shown in Supplementary Materials (Figure S3 and S4). During the calculations, Hubbard parameter $U = 4.6$ eV was applied for both Ti and O atoms to obtain reasonable bandgap values.

Moreover, to verify the alcohol chain length effect on the ligand exchange with $[TiF_6]^{2-}$ complex, additional energy calculations for the F^- ion, methanol, ethanol, n-butanol, and n-hexanol molecules as well as for the $[TiF_6]^{2-}$, $[TiF_5MeOH]^-$, $[TiF_5EeOH]^-$, $[TiF_5ButOH]^-$ and $[TiF_5HexOH]^-$ complexes were performed using PBE functionals within the 20x24x19 Å unit cell to assure minimum 10 Å distance between neighboring molecules. For these calculations, 3 × 3 × 3 k-points grid was used, and geometric optimization was carried out analogical to the crystal structure calculations for most of the structures. Only in the case of $[TiF_5ButOH]^-$ and $[TiF_5HexOH]^-$ their optimization was not entirely performed due to the significant computational times required. Instead, an optimized $[TiF_5EeOH]^-$ structure was taken, and additional $—CH_x$ groups were added based on the optimized *n*-butanol and *n*-hexanol geometries. For these structures, single energy calculations proceeded.

2.4. Electrochemical measurements

To perform Mott-Schottky analysis, 0.02 g of the synthesized nanoparticles were mixed with 0.2 cm^3 of deionized water in an agate mortar, and the obtained paste was applied on the clean fluorine-doped tin oxide (FTO) glass substrate using a doctor blade technique. The as-prepared electrodes were calcined at 450 °C for 2 h with a $5° \cdot min^{-1}$ heating rate. To ensure that calcination does not affect the materials' morphology, additional SEM observation was performed for the selected sample after the whole procedure (see Fig. S9 in Supplementary Materials).

The electrochemical tests for the series of materials were performed in a three-electrode configuration. The FTO covered by the titania layer was the working electrode, Ag/AgCl/0.1 M KCl, and Pt served as reference and counter electrode, respectively, as the electrolyte 0.5 M Na_2SO_4 was used. The solution was 40 min deaerated with argon before measurements, while during the tests, the gas flow was maintained above the solution. The electrochemical impedance spectroscopy (EIS) data was recorded for 45 different potentials selected from the range from + 0.8 V to −1.0 V vs. Ag/AgCl/0.1 M KCl using 10 mV amplitude of the AC signal and 1000 Hz frequency. Those conditions were controlled by the potentiostat–galvanostat Biologic SP-150. The Mott-Schottky plot describing the relation Csc^{-2} vs. E was obtained using the following calculation of the space charge capacitance [39]: $C_{SC} = -1/(2\pi f Z_{im})$, where the imaginary part of the impedance Z_{im} was taken into account, *f* stands for the frequency of AC signal. The flat band potential position was determined based on the tangent's intersection to the Mott-Schottky plot with the potential (E) axis.

2.5. Determination of photocatalytic activity

The photocatalytic activity of the obtained samples was determined in a model reaction of phenol degradation. In a typical run, 0.05 g of the photocatalyst was dispersed inside a 25 cm^3 quartz reactor filled with phenol solution, with a pollutant concentration varying between 20 and 100 $mg \cdot dm^{-3}$ to achieve different phenol/photocatalyst ratios. The obtained suspension was kept in the dark for 30 min to achieve adsorption–desorption equilibrium, followed by 60 min of UV–Vis irradiation. During the whole process, an airflow of 4 $dm^3 \cdot g^{-1}$ was passed through the suspension, and the whole system was thermostated to 20 °C. A Xe lamp equipped with a water filter was used as a light source, and the distance between the reactor border and the lamp was adjusted to keep the measured UV-flux intensity equal to 40 $mW \cdot cm^{-2}$.

Both phenol disappearance and the formation of aromatic by-products were monitored using a high-performance liquid chromatography system (HPLC, Shimadzu LC-6A). During the HPLC runs, an isocratic mobile phase consisting of acetonitrile (Merck), water, and H_3PO_4 (Merck, 85% solution) was used, with their volume fractions equal to 0.7/0.295/0.005, respectively. The C18 5 μm, 150 × 4.6 mm column was used for separation (Phenomenex). Simultaneously, the concentration of total organic carbon after each process was monitored using

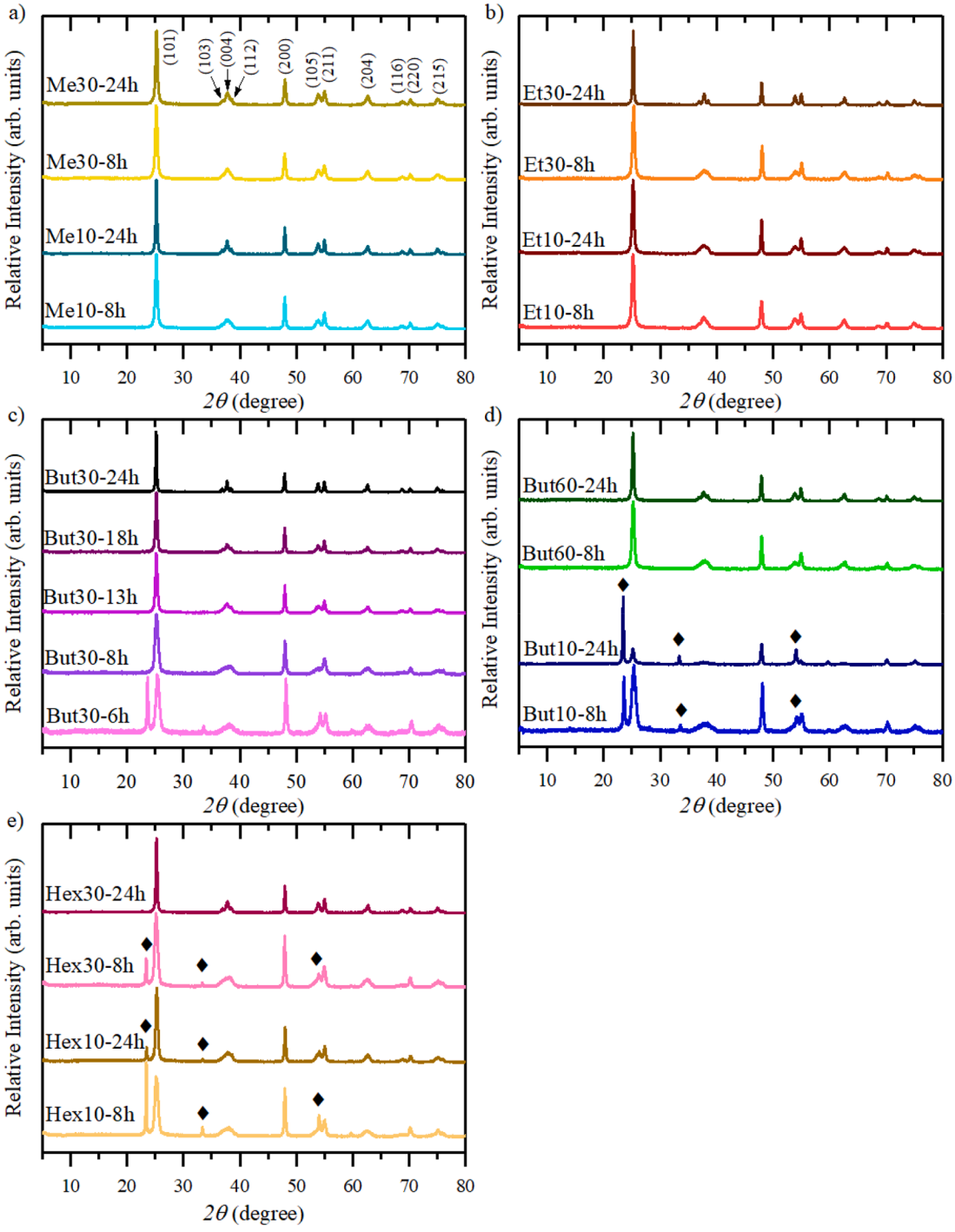

Fig. 1. XRD patterns of samples prepared in (a) methanol, (b) ethanol, (c) 30 cm^3 of n-butanol, (d) 10 and 60 cm^3 of n-butanol and (e) n-hexanol. Throughout the results, reflexes originating from anatase TiO_2 are not marked and are indexed in (a), while cubic $TiOF_2$ signals are marked with rhombus.

the Shimadzu TOC-L analyzer.

3. Results and discussion

3.1. Structural and morphological analyzes

Phase structure and crystallinity of the nanoparticles were analyzed with powder X-ray diffraction (XRD). All obtained results are presented in Fig. 1 and Table 1. Throughout the samples, a formation of anatase TiO_2 was observed and cubic $TiOF_2$ in the case of n-butanol and n-hexanol assisted processes. $TiOF_2$ is known to be an intermediate phase obtained in the presence of HF, which subsequently hydrolyze to TiO_2 [40]. The results showed that this transformation depended on both volume and the type of solvent. The lower content of long-chain alcohols (n-butanol and n-hexanol) stabilized the $TiOF_2$ phase and only increased their amount, promoting further conversion to TiO_2. Moreover, an additional effect of the alcohol was observed in terms of crystallite growth and the amount of amorphous phase presence inside obtained materials. In the case of pure TiO_2 particles, both increasing alcohol amount and changing it to the shorter chain alcohol promoted the creation of more crystalline particles at the early stage of the process. On the other hand, the opposite approach resulted in a continuous crystallinity rise, which covered a broader parameter range. It is generally followed by the crystallites' growth, which is shown in Table 1, calculated for the size along the *l* crystallographic direction. A visible dependence of both factors on the type and the volume of alcohol suggests that its presence affected the growth rate of the TiO_2 nanocrystals. As a consequence, it further indicates that the alcohol role is not limited solely to co-stabilization of the {001} structure together with fluorine, as previously shown [34,41].

Furthermore, XRD patterns showed a characteristic broadening of the signals originating from the (004) and (105) planes of anatase, which suggested that the size of the nanoparticles was significantly reduced in the *l* direction [42]. That was further confirmed by the SEM observations, as shown in Fig. 2. The formation of 2D anatase nanoparticles resulted directly from the HF presence during the synthesis, which stabilizes the {001} facets and promotes growth in the *hk* directions, according to the Gibbs-Curie-Wulff theorem [5]. For the well-defined 2D nanoparticles, their observed heights are in agreement with the calculated crystallites size using the (004) reflection, proving that the obtained particles should be single crystalline with {001} facets exposed at the top/bottom (see Fig. S7 in the Supporting Materials). Nevertheless, some differences between samples were noticed. It can be seen that both increasing alcohol content and changing it to shorter-chain alcohol produced smaller and less platelet materials. It was primarily observed for the 8 h reactions, while for the 24 h, increased alcohol amount inhibited the particles' further growth. Moreover, for the reactions involving methanol and 10 cm^3 of ethanol extremely fine particles, without expected 2D morphology were observed and formation of well-defined nanosheets occur only for the ethanol when prolonging the synthesis time. This effect was not observed for the *n*-butanol and *n*-hexanol series.

It is known that particles size is influenced by their nucleation rate [43] and therefore is dependent on both alcohol amount and its type, with the highest nucleation rate observed for the MeOH and EtOH series. On the other hand, subsequent TiO_2 growth in the HF-assisted synthesis is known to be a result of fluorine mediated dissolution-recrystallization process [40,44–45], which could be schematically described by the following equation:

$$TiO_2 + 6HF \leftrightarrow [TiF_6]^{2-} + 2H_2O + 2H^+$$

In this process, titanium is reversibly transferred between its solid oxide form and dissolved ion/molecule, preferably coordinated with 6 ligands in the form of bipyramid. The above reaction illustrates the behavior of samples Et10-8h and Et10-24h, showing fast nucleation of TiO_2 nanoparticles, which further rearranged to form well-defined nanosheets as the reaction time was prolonged. However, despite the necessity of HF presence to etch TiO_2 structure, formation of $[TiF_6]^{2-}$ is questionable, and the presence of other, less fluorinated Ti species was also reported [46]. An alcohol exchange with halide ligands is primarily known to be possible under solvothermal conditions [47–48]. Therefore, we have computationally verified if alcohol chain length could influence such process by replacing single fluorine from $[TiF_6]^{2-}$ octahedra with alcohol molecules.

$$[TiF_6]^{2-} + ROH \rightarrow [TiF_5ROH]^- + F^-$$

As shown in Fig. 3, a visible effect between the short and long-chain alcohols can be observed, with ethanol and methanol requiring lower energy for such reaction to occur. A possible exchange of F^- with MeOH and EtOH at relatively mild conditions could especially promote further TiO_2 condensation through an ether elimination mechanism [49–50], which would increase its nucleation rate. Moreover, this seems especially possible while considering an increased steric hindrance together with the alcohol chain length, which, on the other hand, should slow

Table 1
Structural parameters of the obtained samples.

Sample name	Anatase crystallite size along with the [0 0 1] direction (nm)	Anatase lattice parameters (Å)		Phase content (w/w %)		Amorphous phase content (w/w %)
		a,b	*c*	TiO_2 (anatase)	$TiOF_2$	
Me10-8h	14	3.787	9.512	100	–	37.5
Me10-24h	23	3.786	9.508	100	–	18
Me30-8h	13	3.788	9.504	100	–	24
Me30-24h	15	3.788	9.506	100	–	35
Et10-8h	13	3.789	9.513	100	–	39
Et10-24h	17	3.787	9.511	100	–	16
Et30-8h	16	3.790	9.522	100	–	32
Et30-24h	30	3.786	9.505	100	–	14
But10-8h	9	3.796	9.558	87	13	51
But10-13h	14	3.791	9.522	91	9	39
But10-24h	12	3.801	9.560	49	51	33
But30-6h	10	3.792	9.538	77	23	64
But30-8h	12	3.790	9.526	100	–	66
But30-13h	17	3.789	9.514	100	–	58
But30-18h	21	3.788	9.505	100	–	46
But30-24h	33	3.787	9.506	100	–	19
But60-8h	15	3.789	9.518	100	–	33.5
But60-13h	22.5	3.787	9.513	100	–	25.5
But60-24h	21	3.787	9.509	100	–	23
Hex10-8h	11	3.789	9.527	85	15	39
Hex10-24h	16.5	3.791	9.523	97	3	58
Hex30-8h	12	3.788	9.520	94	6	54
Hex30-24h	27	3.787	9.508	100	–	21

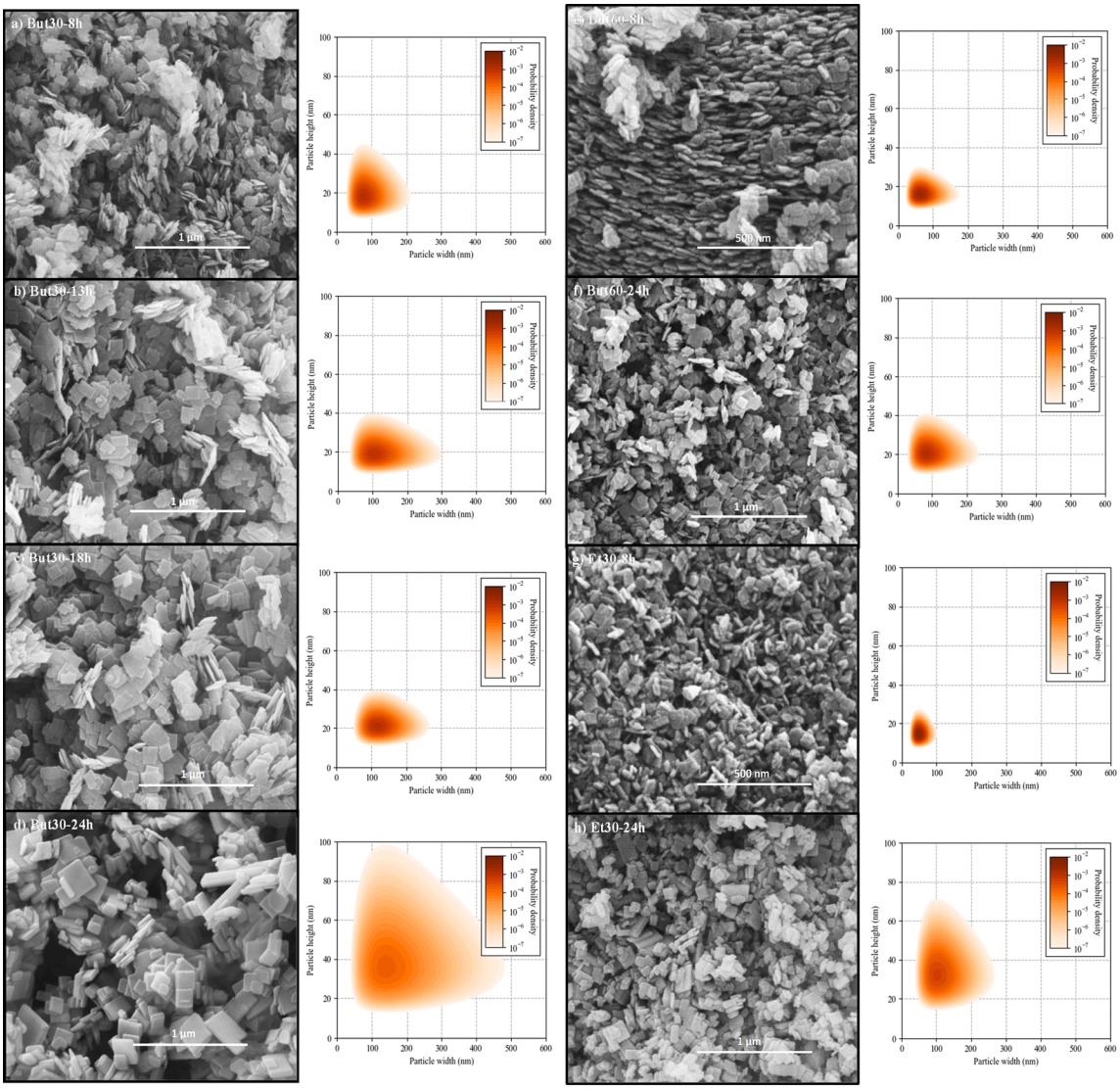

Fig. 2. SEM images of 2D TiO_2 nanosheets and graphs of their size distribution. Other SEM images are presented in Supporting Materials (Fig. S2).

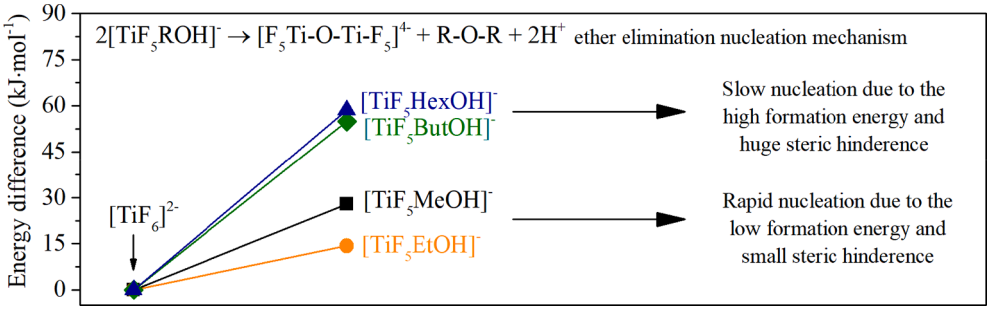

Fig. 3. Obtained energy difference due to the exchanging F^- to ROH ligand in the $[TiF_6]^{2-}$ complex.

down such a process [51]. For the n-butanol and n-hexanol assisted processes, this could promote slower nucleation of the TiO_2 nanoparticles, which could grow into well-defined nanosheets. Therefore, low energy required to exchange the fluorine, together with small steric hindrance, could explain observed morphology differences, especially for the 8 h processes, as a result of increased nucleation rate through ether elimination (2D morphology for But30 and Hex30 series vs. ultrafine, but irregular particles for Met10 and Et10).

On the other hand, a significant increase in alcohol content (Met30, Et30, and But60) can promote subsequent alcohol condensation in the presence of HF to produce additional H_2O molecules [43].

Therefore, the TiO_2 structure became more stable, and the dissolution-recrystallization process became slowed down, as observed mainly for samples Met30-8h and Met30-24h. Moreover, increased H_2O content results in less platelet particles' formation due to gradual hydrolysis and condensation of fluorine-terminated TiO_2 facets in the aqueous environment [52].

Described results showed that alcohol effect is not limited to

influence on F^- chemisorption and especially its volume is also affecting the kinetics of TiO_2 growth. Specifically, as shown in Fig. 4, the stable formation of highly platelet particles in the adapted conditions can be obtained when ROH/TBT ratio is between 3.5 and 6.5. Furthermore, for this reaction system, the kinetics of TiO_2 nucleation depends on the possible alcohol exchange with fluorine, which should promote faster nucleation through subsequent ether elimination. For the lower alcohol contents, $TiOF_2$ stabilization may occur mainly for samples prepared with n-butanol and n-hexanol. Moreover, less platelet particles are formed for the higher alcohol amounts through increased ROH condensation to give H_2O.

3.2. Surface properties

Since semiconductors' surface properties are critical in the context of their practical applications, the prepared TiO_2 samples were further analyzed in terms of their surface development and composition. Fig. 5 shows the isotherms of nitrogen adsorption-desorption for the synthesized nanoparticles in the range of p/p_0 from 0 to ~1.

The obtained isotherms showed characteristic features of the type IV family [53], with the reversible mono- and multilayer adsorption in the lower range of p/p_0, followed by the hysteresis loop for higher pressure values. For all samples, a visible decrease in the adsorbed volume with the reaction time was noticed, especially for the lower part of the isotherm, which is in agreement with the observed crystal growth and crystallinity increase of the material. Moreover, both H1 (adsorption limit for high p/p_0 values) and H3 (no limit) isotherm types are observed, with a significant effect of the introduced alcohol [54]. The type H3 loop is ascribed to materials with aggregates of plate-like particles giving rise to slit-shaped pores and therefore corresponds well with the 2D morphology observed, especially for the But30 and hexanol series [27]. Moreover, since the hysteresis were observed for high p/p_0 values for these samples (mostly > 0.85), it was found that most of the pores' volume was formed by the inter-aggregate macro/mesopores created between nanocrystalline platelets. On the other hand, an introduction of methanol results in the type H1 loop, which is in agreement with their ultrafine but less platelet morphology, as revealed by the SEM analysis. Furthermore, smaller pores' formation was observed for these samples with more narrow distribution (see Fig. S8 in the Supporting Materials for distribution graphs). The surface development and pore size distribution followed the SEM and XRD results, showing an alcohol influence on the obtained samples' adsorption behavior. Detailed sorption measurements, including calculated BET surface area, total pore volume, and average pore size, are given in Table 2.

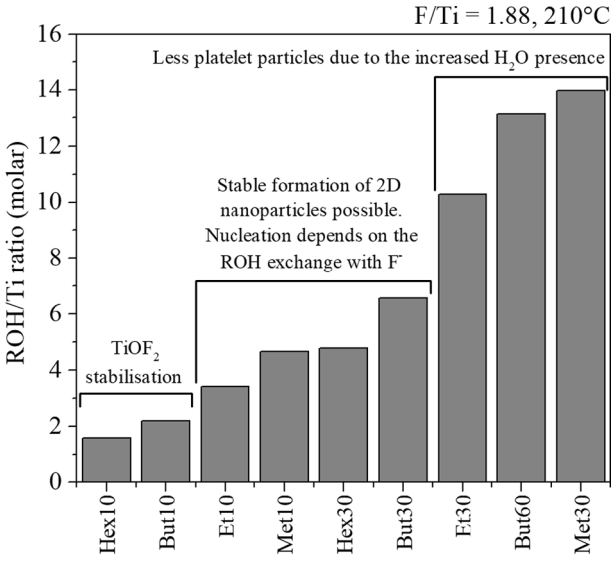

Fig. 4. Schematic representation of the observed alcohol effect on the formation of {001} exposed anatase nanoparticles after arranging them in accordance with the ROH/Ti ratio.

Simultaneously, selected samples were analyzed with XPS to determine their surface composition. Due to the strong Ti—F interactions, HF addition can affect the surface structure of the growing TiO_2 and, consequently, influence their final properties [56]. It can be observed even after initial washing with a basic solution, such as NaOH. The presence of both Ti and F on the surface was demonstrated in XPS spectra of all samples, and the summation of their characteristics is presented in Table 2.

As shown in Fig. 6, for most analyzed samples, well-defined Ti^{4+} doublet can be observed around the 458.5/464 eV, which corresponds to the TiO_2 surface structure. However, throughout the samples, both signals at the lower and higher energies can be observed, which can be ascribed to the Ti^{3+} states, as well as to the possible Ti—F bonds, respectively [57,58]. Concerning the solvent effect, it was found that alcohol type and its amount affect surface Ti—F bonding and possible Ti reduction. Mainly, methanol introduction resulted in a visible surface fluorination and little (or zero) presence of the stoichiometric TiO_2. This can be seen as a consequence of very fast nucleation, which further leaves the remaining HF to react and etch the particle's surface. On the other hand, most of the ethanol and n-butanol assisted samples showed clear TiO_2 surfaces with only some differences in their fluorination. For this series, it can be observed that an increase in the alcohol content decreases the amount of surface fluorine. It is known that fluorinated TiO_2 nanosheets undergo gradual hydrolysis and further condensation to the 3D particles due to the hydrothermal reaction in the H_2O environment [52]. Therefore, both less platelet character of the But60 and Et30 series and their less fluorinated surface should especially result from increased H_2O presence, comparing the But30 and Et10 series, respectively.

Furthermore, a significant amount of the Ti^{3+} species were observed in the case of sample Et30-24, which might result from the surface presence of oxygen vacancy induced by the free HF in the H_2O-rich environment [59]. It was followed by the visible valence band tailing observed for this sample, which is shown in Fig. 7. Finally, for the Hex30-24 sample, a series of additional Ti—F states is observed along with the TiO2 signal, which might inhibit TiO_2 hydrolysis and stabilization of the intermediate $TiOF_2$ structure for the longer chain alcohols, as revealed by the XRD analysis.

3.3. Optical properties and electronic structure

DR/UV–Vis spectra of the prepared TiO_2 nanosheets are presented in Fig. 8. For all samples, the main absorption around 3.2 eV was observed, ascribed to the electron transfer from the valence band to the conduction band in the pure anatase structure. No increase of absorbance, which would overlap with this transition was observed, indicating no additional bulk states directly above/below the valence/conduction band edge. However, a visible difference was noticed within the bandgap of the samples. Especially, samples that were found to possess higher amounts of Ti—F surface bonds (Met series, Et10-24h, and Hex30-24h) showed visible enhancement either around the 500 nm or in the whole visible-NIR regions of the spectrum. This is in agreement with other studies describing the $TiOF_2$ absorbance spectrum, with the characteristic band at approx. 480 nm [33]. A similar but smaller effect could be observed for the sample Et10-24h. On the other hand, the samples prepared with n-butanol and 30 cm^3 of ethanol showed a different behavior with a monotonous absorbance increase towards the longer wavelengths. Especially for the But30 series, the appearance of two bands at 2.2 and 1.1 eV was noted, while the far-UV absorbance was simultaneously decreasing, suggesting a change in the amount of O 2p bonding orbitals (these are defined as being within the Ti_3O plane [60]). In the case of series But60 and Et30, no well-defined band at 2.2 eV was

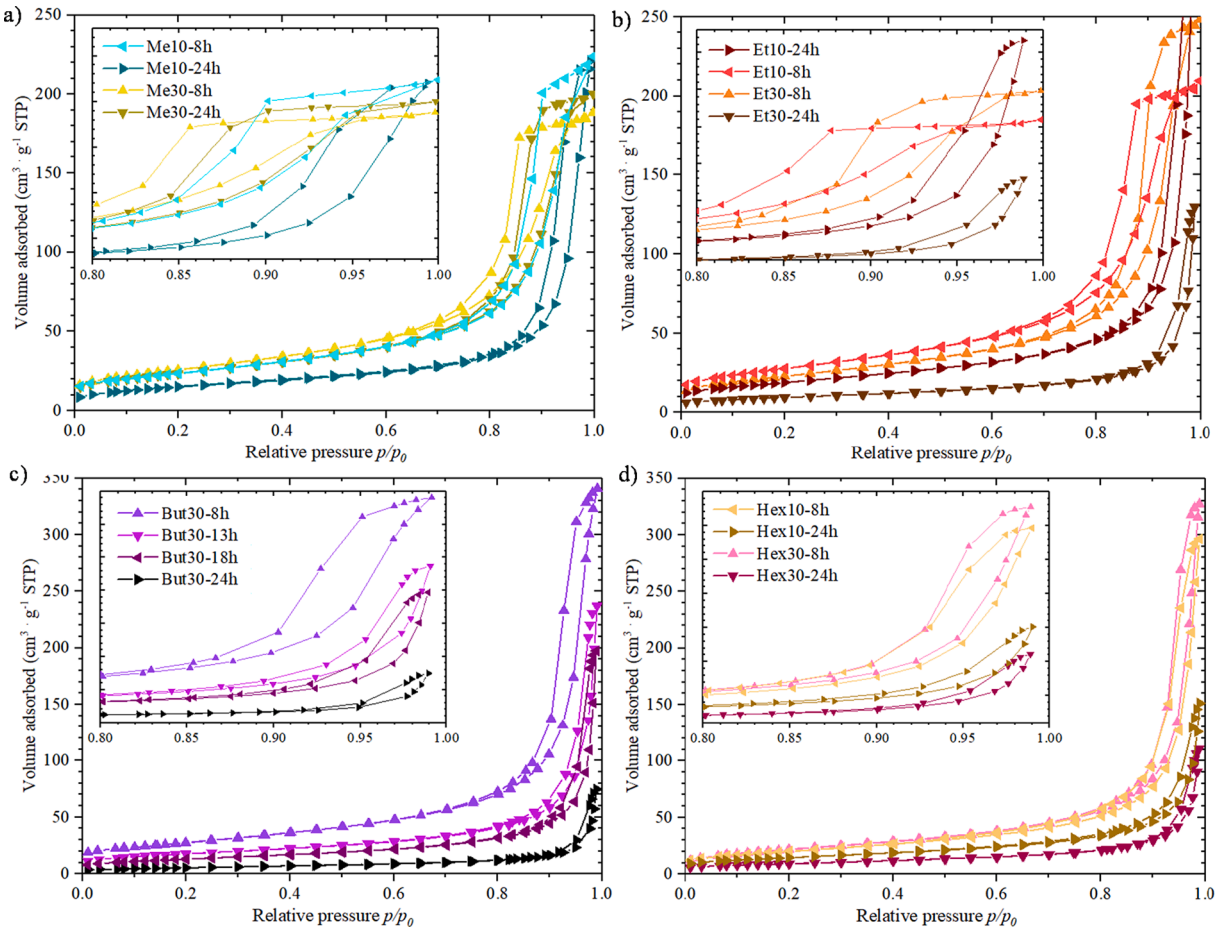

Fig. 5. Low-temperature N_2 sorption isotherms measured for the obtained samples. Inside are given the close-up views of the high p/p_0 regions.

Table 2
Surface characteristics obtained from the N_2 sorption and XPS analysis.

Sample name	Sorption			XPS			
	S_{BET} ($m^2 \cdot g^{-1}$)	V_{pores} ($cm^3 \cdot g^{-1}$)	d_{Pores}[1] (nm)	Ti^{3+}/Ti^{4+}	Ti-F/Ti-O	Total F/Ti	VB edge (eV)
Me10-8h	85	0.35	13.3	0	5.87	0.18	1.97
Me10-24h	54	0.34	21.8	n.d.	n.d.	n.d.	n.d.
Me30-8h	94	0.29	9.8	No TiO_2	6.3	0.11	2.22
Me30-24h	85	0.31	11.7	n.d.	n.d.	n.d.	n.d.
Et10-8h	100	0.33	10.6	0	0.32	0.12	1.84
Et10-24h	68	0.49	25.9	0	0.26	0.15	1.79
Et30-8h	83	0.39	14.6	0	0.06	0.075	2.08
Et30-24h	34	0.20	23.0	0.19	0	0.063	~0
But30-8h	99	0.53	17.8	0	0.13	0.15	2.12
But30-13h	62	0.37	22.5	n.d.	n.d.	n.d.	n.d.
But30-18h	47	0.31	23.2	n.d.	n.d.	n.d.	n.d.
But30-24h	19	0.12	22.7	0	0.18	0.13	1.89
But60-8h	80	0.37	15.4	0	0.17	0.24	2.01
But60-13h	47	0.37	27.3	0	0.10	0.066	1.74
Hex10-8h	73	0.46	19.6	n.d.	n.d.	n.d.	n.d.
Hex10-24h	52	0.24	17.0	n.d.	n.d.	n.d.	n.d.
Hex30-8h	79	0.51	20.9	n.d.	n.d.	n.d.	n.d.
Hex30-24h	42	0.17	20.3	0.05	0.52	0.11	1.93

[1] Average pore size is determined for all macro, meso, and micropores together to represent a change in the overall size distribution. For the detailed results of the observed pores' size, please see the Supporting Materials.

observed, while the absorbance change within the UV region was very limited, especially for the Et30 series. However, the absorbance rise was still observed up to $\lambda = 1100$ nm for these samples.

Since almost all samples obtained from ButOH and EtOH series were found to be pure 2D anatase, with the majority of the TiO_2 surface signals, their absorbance should be connected with the possible point defects in their crystal structure. Therefore, to better understand their behavior, possible electronic structures using Density Functional Theory (DFT) method have been simulated. The calculated density of state distributions is shown in Fig. 9, including bulk and (0 0 1) surface slab

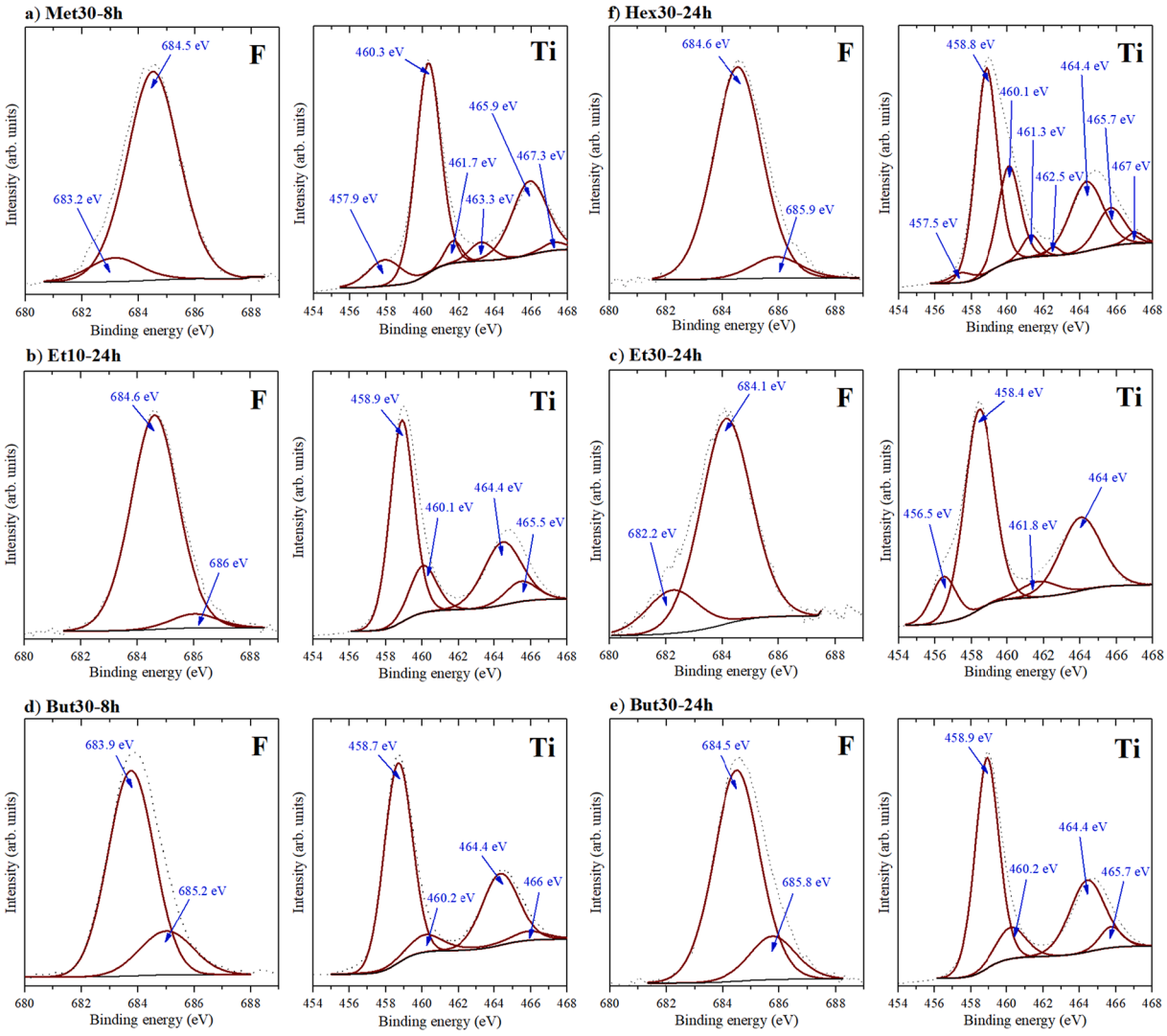

Fig. 6. The observed XPS signals originating from Ti and F atoms together with their deconvolution for selected anatase samples.

models, both pure and with possible defects considered. The obtained results showed a formation of well-defined midgap states resulting from the oxygen removal due to the presence of unpaired d electrons on the Ti atom, forming Ti^{3+} ions. For a bulk structure, these states are located approximately between 1 and 2 eV from the valence band edge and, therefore, would fit very well to the bands observed in the UV–Vis spectrum of the But30 series. The formation of oxygen vacancies inside the bulk structure can be further reasoned by the structural change around the vacancy, which would cause O atoms to displace themselves from the Ti_3O plane, therefore decreasing the number of highly bounded orbitals responsible for the UV absorption below 300 nm. Finally, no Ti^{3+} states observed in the XPS spectrum of this sample fit well the above description.

However, similar results were not observed in series But60 and Et30, suggesting that their structures differ from the But30 samples. Significantly, the lack of a band at 2.2 eV and strong light absorption at $\lambda =$ 250 nm suggest that no oxygen vacancies are present in their bulk structure. None of the calculations considered in Fig. 9a could explain well the obtained XPS/UV–Vis results. Therefore, the effect of the {0 0 1} surface structure was taken into consideration. The performed calculations, especially the formation of surface oxygen vacancies, seem to be in good agreement with the obtained results for sample Et30-24h, which showed both the surface presence of Ti^{3+} and the valence band tailing. It also agrees with the study of Linh et al., who have shown that the mid-gap states created as the result of oxygen vacancy at the (0 0 1) surface could shift according to the Ti-O interactions [61] (affected during calculations by the arbitrary applied *U*). Assuming the formation of a more continuous distribution of these mid-gap states in reality and the pinning of the Fermi energy at their level, this seems to be a reasonable interpretation of the observed valence band tail in the XPS spectra for Et30-24h. In this case, the absence of additional maxima on the UV–Vis spectrum could be due to the bandgap reduction on the surface and their relatively low amount compared to the whole structure.

On the contrary, But60 samples and sample Et30-8h did not show any significant valence band tailing or Ti^{3+} presence. Therefore, their characteristics should result from different features. As an alternative explanation, we focused on the F ions present in the sample's surface region. Fluorine enhanced the n-type properties of TiO_2 and could create additional electrons inside the anatase structure [62–63]. These electrons can be a reason for the rising absorbance up to the IR spectrum due to their localization inside the conduction band states [64]. The interplay between TiO_2 stoichiometry and F presence was studied by Seo et al., who have shown that fluorine passivates the defects states caused by O deficiency and could contribute to the conduction band electrons without changing the bandgap of anatase [63]. It seems to be a plausible explanation of the UV–Vis behavior of these samples and is in agreement with our calculations, showing that F_I presence below the (0 0 1) surface does not change the material's electronic structure significantly.

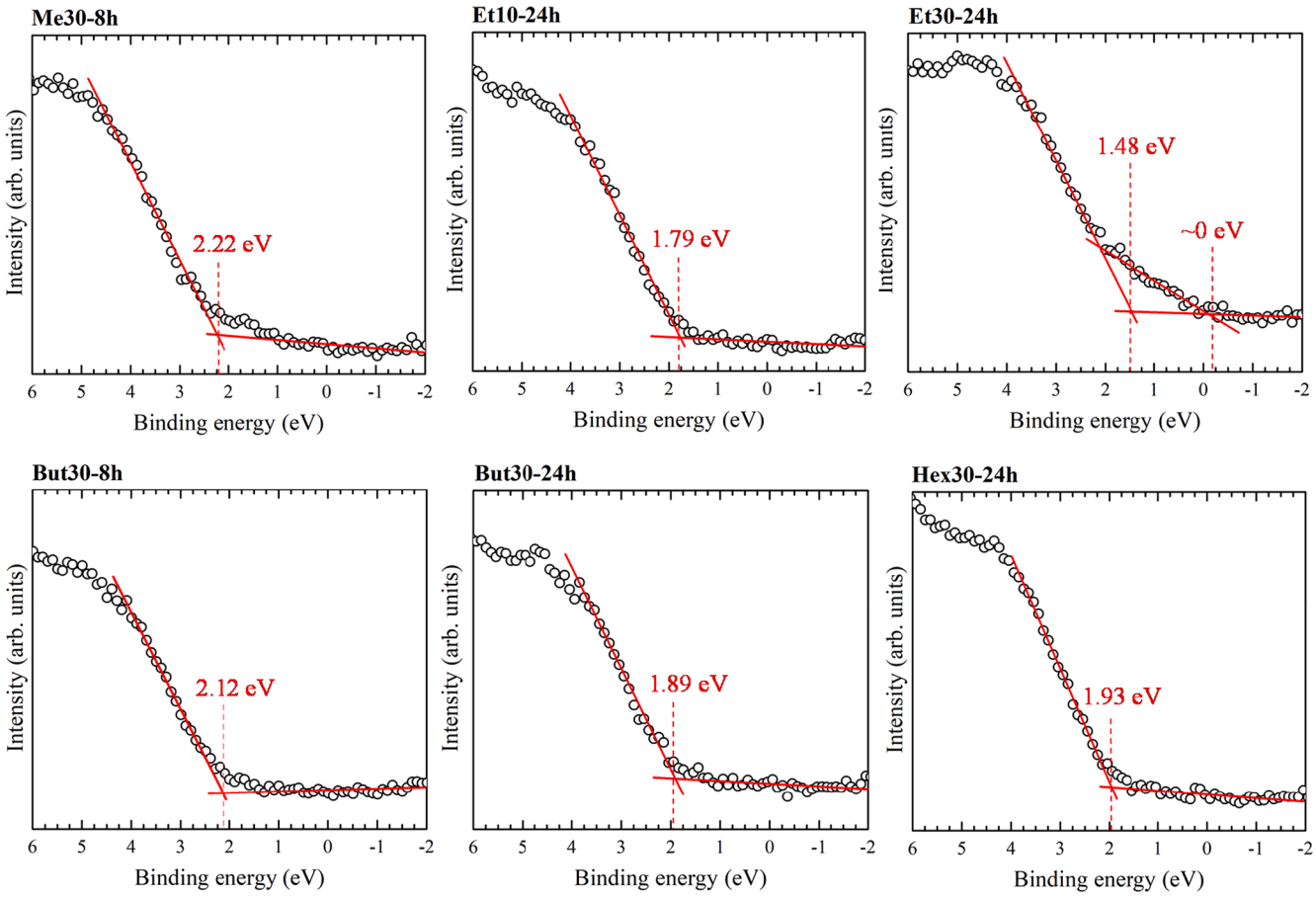

Fig. 7. Observed valence band edges for the selected anatase samples.

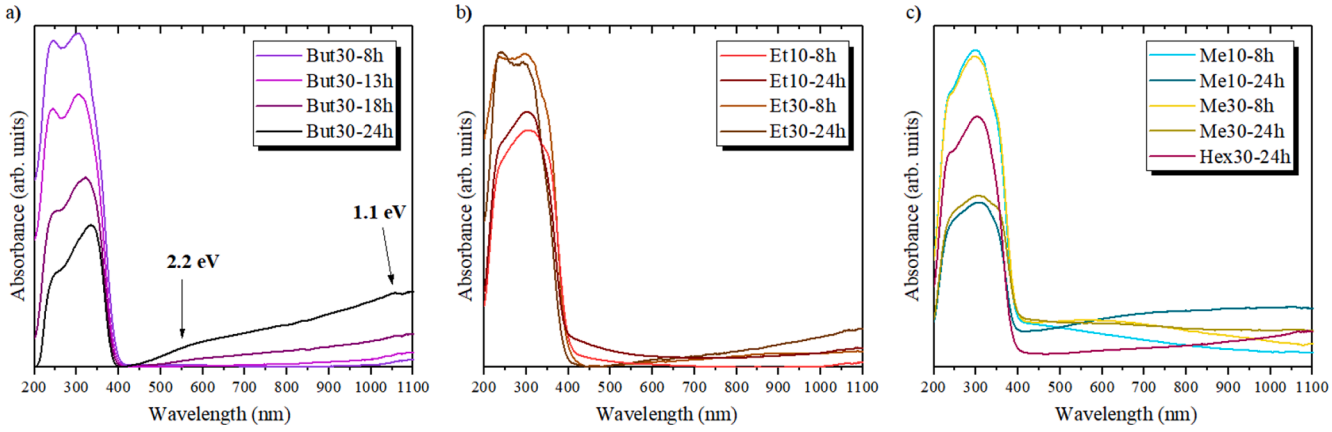

Fig. 8. DR/UV–Vis spectra of TiO_2 nanosheets obtained using (a) 30 cm^3 of n-butanol, (b) ethanol, (c) methanol, and 30 cm^3 of n-hexanol.

3.4. *Electrochemical studies*

Fig. 10 shows the band positions of pure TiO_2 samples, based on Mott-Schottky and UV–Vis analysis of the obtained nanosheets. The determined flat band potential is regarded as a significant quantity for semiconductor electrodes because it determines the position of band edges at the interface between the electrode material and electrolyte [65]. Consequently, the energy of conduction-band electrons, and taking into account bandgap energy, the valence band edge position can be estimated. It was found that for the Me10 and But30 series, no visible effect of the reaction time onto the location of energy bands was present, while for both But60 and Et30 series, a distinct change was observed, with longer preparation time resulting in the negative shifting of the bands' edges. It can result from lowering the surface content of fluorine with a longer synthesis time for these series, while F ions are known to cause bending of the conduction band edge [66–67]. Indeed, the band positions seem to be fluorine-dependent, and a significant downshift of the conduction and valence bands was observed for the most fluorinated samples, name But60-8h, Me10-8h, or Et10-24h. Meanwhile, samples But30-8h and But30-24h possess almost the same band positions and similar fluorine content.

As it is known, the band position influence significantly the charge transfer between the photocatalyst and the reacting species. The degradation of organic pollutants is connected with the generation of

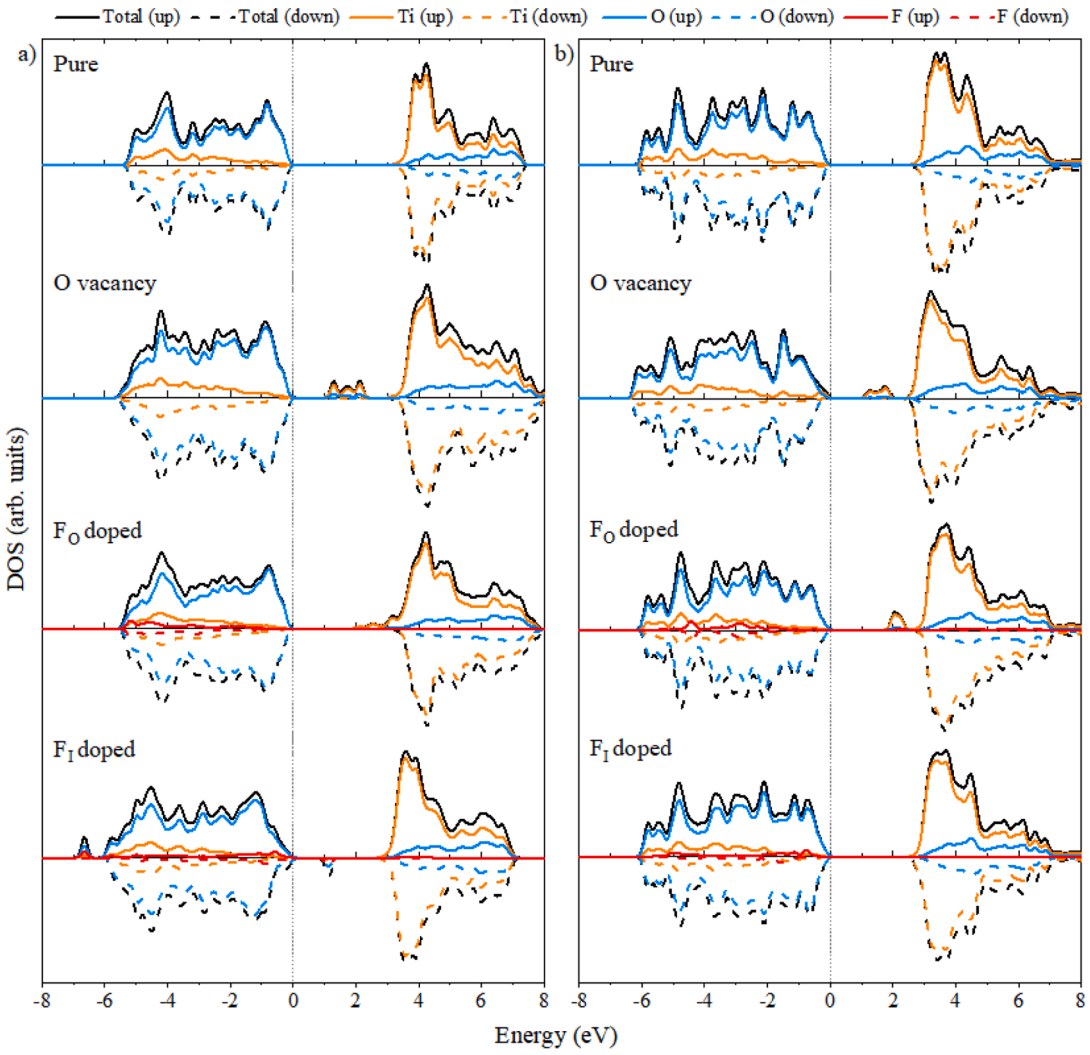

Fig. 9. The calculated density of states (DOS) distributions for (a) bulk and (b) (0 0 1) surface slab models of anatase. Shown results are for pure structures as well as oxygen-deficient anatase, structures with fluorine-doped in the place of oxygen (F_O), and anatase with fluorine-doped in interstitial position (F_I).

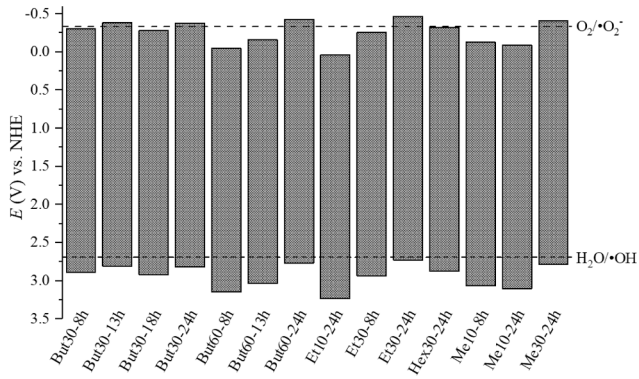

Fig. 10. Band edge positions of TiO_2 nanoparticles determined from the Mott-Schottky analysis and UV–Vis absorption. The length of the grey stripes corresponds to the bandgap energy values. Redox potentials for radicals formation are adapted from [68].

reactive oxygen species, especially $^{\bullet}OH$ and $^{\bullet}O_2^-$ through water oxidation and reduction of the adsorbed oxygen on the photocatalyst surface [69–70]. In this regard, it was found that depending on their morphology and surface characteristics, the solvothermal reaction conditions influenced the photocatalytic activity of these materials, which will be discussed further.

3.5. Photocatalytic activity measurements

The photocatalytic activity of the obtained materials were tested in the reaction of phenol degradation. The results are shown in Fig. 11, in which sample But30-13 h was omitted due to all characteristics being analogical to the other three samples from this series. It was observed that the remarked rate of phenol disappearance exhibits an extreme variation between the samples, ranging from $k = 0.118$ min^{-1} to 0.019 min^{-1}. Considering performed characteristics and observed phenol removal efficiency, obtained samples can be classified into four categories: well defined 2D nanoparticles, which allow efficient phenol degradation (series A), 2D nanoparticles, which photocatalytic activity was compromised, and no formation of *ortho*-hydroxyphenol (catechol) was observed (series B), non-2D nanoparticles (series C) and TiO_2/$TiOF_2$ mixture samples (series D). Considering the $TiOF_2$ presence, it was reported that it could enhance the visible light activity of the TiO_2 materials [43,71]. However, when irradiated with UV–Vis light, its activity is poor, comparing with anatase [10,33]. It is in agreement with our previous study as well as with control measurements performed for samples But10-8h, But30-6h, Hex10-8h, and Hex10-24, which have shown no positive effect of the $TiOF_2$ presence on the photocatalytic performance (see SI Fig. S10 for more details). Therefore, these samples were not

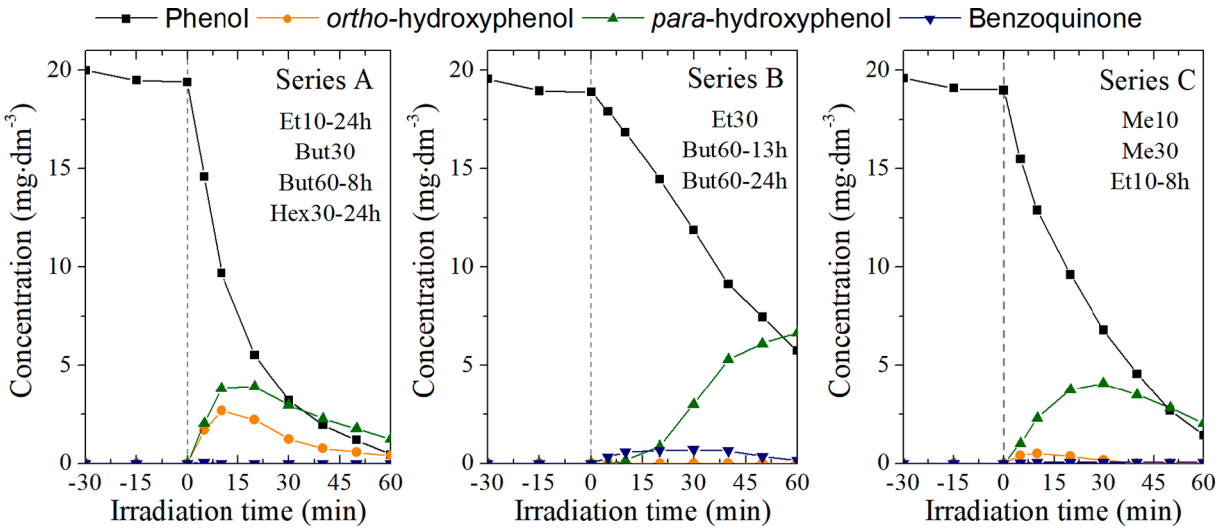

Fig. 11. Mean results of the degradation of 20 mg·dm^{-3} phenol solution for the obtained samples after grouping them in similar-behaving series. Detailed results for each sample are presented in Supporting Materials (Fig. S11).

discussed in detail.

Focusing on the pure TiO_2 samples, series A seems to work "properly", and the obtained rate constants are comparable or higher than presented in the literature. For example, the photocatalytic activity in UV–Vis light of these 2D photocatalysts is similar to doped TiO_2 [18,72–73], or anatase nanosheets/bipyramids from the solvothermal synthesis in water [74]. Mino et al. have shown TiO_2 anatase nanostructures with dominant {001} or {101} facets obtained from solvothermal synthesis connected with lyophilization. The most efficient photocatalyst was bipyramidal nanoparticles; however, they achieved only ca. 10% phenol degradation after 60 min of the photodegradation reaction [74]. On the other hand, Sui et al. have presented Ti^{3+} self-doped TiO_2 single crystals with internal pores, which decomposed about 100% of phenol in 35 min when truncated octahedral bipyramid structured TiO_2 was used as the photocatalyst [75]. However, both studies do not present phenol mineralization efficiency.

Considering series B, its behavior was quite surprising both due to the markedly lower phenol degradation and significant change in the by-products formation. Moreover, a weak dependence between the rate constant and surface area of the photocatalyst was noted for this series. From the overall results, this effect seems to be connected with three previously noticed features (i) the low amount of surface fluorine observed for these samples, (ii) an upward shift of the band position for longer synthesis time, and (iii) the possible surface defectivity, especially connected with a surface excess of electrons (Ti^{4+} reduction on the surface of Et30-24h sample). Significantly, the latter could influence the formation of reactive oxygen species on the photocatalyst surface. As reported by Ma et al., the anatase {001} surface should preferentially localize photogenerated holes on the surface bridging O atoms [31], which is a position also suitable to generate $^{\bullet}OH$ from water [70]. In this case, both cathodic band shift and electron accumulation on the surface (Ti^{3+} states) could prevent h^+ from localization on the surface O and further H_2O oxidation. This can explain a distinct decrease of k since {001} surface should not be able to accumulate electrons directly on the surface Ti atoms [31]. Therefore, the whole process starts to be limited by the energy barrier of charge carrier transfer to the surface rather than further reactions with different species. This is in agreement with the minimal effect of the surface area on the activity of these samples. Moreover, inhibition of the $^{\bullet}OH$ formation would explain the absence of catechol since its creation should result from $^{\bullet}OH$ attack close to the phenol adsorption site [33].

Finally, samples from series C exhibit quite good photocatalytic performance; however, observed phenol removal was still visibly slower than in series A. Moreover, no catechol formation was noticed for this series. These results suggest that samples from series C behave differently than series A and B, which should especially result from their different morphology. Comparing it with series A, it was observed that the situation is opposite to series B, and a relatively high amount of fluorine on the surface, together with the lack of defined surface defects, have led to high k values for this series.

All of the performed photocatalytic tests were followed by analyzing total organic carbon (TOC) to determine the obtained samples' mineralization ability. Concerning 2D nanostructures, it is known that reaction at the {001} facet is driven by photogenerated holes and further by $^{\bullet}OH$ attack to phenol molecule. Therefore samples from series A have shown a noticeable dependence on the available surface area (calculated as a ratio between undercoordinated surface O atoms, being active sites for $^{\bullet}OH$ formation, and the total amount of organic C at the start of the process). Furthermore, samples from series B achieved visibly lower per-surface mineralization, which agreed with their compromised activity, as observed before. On the other hand, series C showed good mineralization efficiency, especially when considering their lower rates of phenol removal, when compared to series A. These differences could especially result from the alternate surface structure of series C samples, which could enhance the formation of other reactive species, such as $^{\bullet}O_2^-$ radicals that could help mineralize aromatic compounds. The comparison between mineralization efficiency of described series is presented in Fig. 12.

From the overall results, it was found that a maximum TOC removal of 69% is observed for series A and 81% for series C. These results are promising considering the difficult and complex mechanism of phenol degradation and comparing to similar studies, which usually report photocatalytic phenol mineralization below 50% [72,74,76].

Furthermore, it is worth noting that quite different mineralization efficiency for all series clearly shows that the relationship between created phenol's by-products and TOC removal is morphology-dependent. Both samples from series B and C promoted the formation of hydroquinone as almost only intermediate, while their mineralization ability was significantly different. On the other hand, series A can achieve relatively high mineralization while the presence of catechol was observed during the process. In this study, no correlation between particle size and selective hydroquinone or catechol production was noticed since the smallest nanoparticles were obtained for series C, while both series A and B included samples with different sizes. Although Suhadolnik et al. and Turki et al. have presented phenol mineralization mechanism going through benzoquinone formation [27,77], the

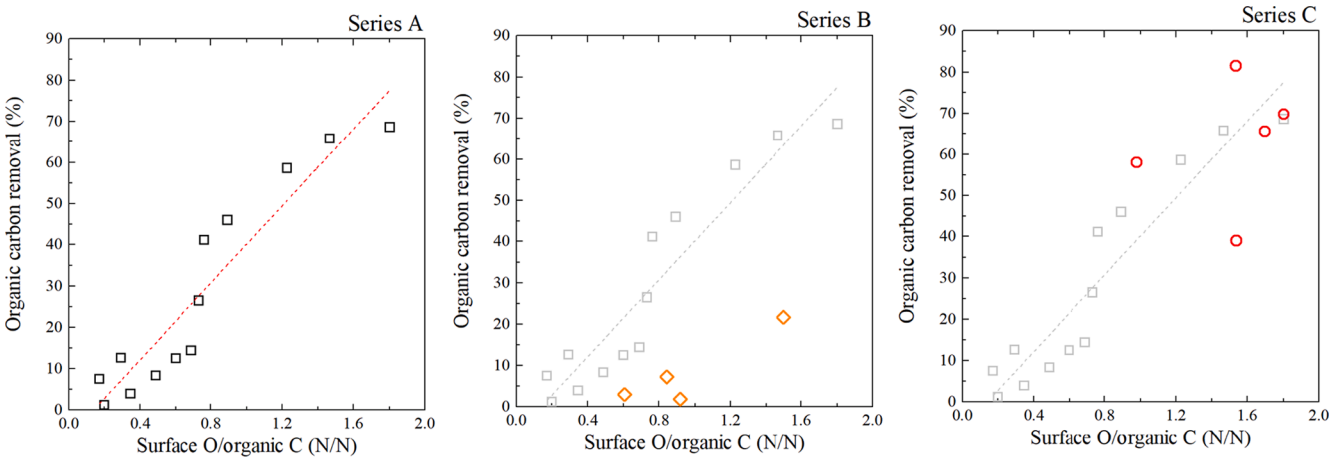

Fig. 12. The dependence between the observed mineralization ability and obtained samples on the surface area of the photocatalyst (recalculated as a ratio between undercoordinated surface O atoms and the total amount of organic C at the start of the process).

presence of benzoquinone was observed only for the series B, which was followed by significant inhibition of the mineralization process.

Therefore, it was assumed that facet exposition influence both of these processes. As highlighted before, it should especially result from differences in the generated reactive oxygen species and their further reaction with phenol. The {001} exposed particles are primarily reactive toward $^{\bullet}OH$ generation, and therefore the formation of $^{\bullet}O_2^-$ should be unfavored for these nanoparticles [31]. This allows to achieve a high phenol removal rate; however, mineralization is relatively lower since hydroxyl radicals are worse ring-opening agents than $^{\bullet}O_2^-$. For such materials, the final TOC removal depends strictly on the available surface area.

On the contrary, when h^+ transfer and further reaction at the surface became suppressed (series B) degradation process became significantly hindered for such materials. On the other hand, despite achieving quite good mineralization efficiency for the {001} exposed nanoparticles, the series C samples generally allow to obtain higher TOC removal, regardless of the simple phenol degradation rate. Specifically, sample Me10-8h, also with high surface area, achieved 81% of organic carbon removal while possessing less defined morphology, highly defected surface structure, and slower removal of phenol itself (see Fig. S11 in Supporting Materials). Assuming that morphology change for these samples allowed to generate superoxide radicals effectively, it became reasonable that higher TOC removal could be obtained. Moreover, surface O defects might promote $^{\bullet}O_2^-$ generation for such samples [78]. The defect-enhanced activity was not observed for series B, suggesting similar morphology dependence of such phenomenon. Analogically, this could be explained based on the different charge carriers' localization and further ROS generation between the series. As a final comparison, the activity of commercial P25 and other anatase nanoparticles obtained from $TiCl_4$ without any structure-defining additives was analyzed and compared to the most active 2D sample – But30-8h. As shown in Fig. 13, a higher phenol degradation rate constant was noticed for {001} nanosheets, with a higher amount of *para*-hydroxyphenol (hydroquinone) and lower mineralization ability measured as a TOC removal compared to commercial TiO_2 P25 and TiO_2 from $TiCl_4$.

3.6. Final remarks on the photocatalyst structure

Focusing on the photocatalytic activity of the obtained nanosheets, the overall results suggest that it depends on the {001} ability to produce $^{\bullet}OH$ radicals involved in phenol degradation. In this regard, the

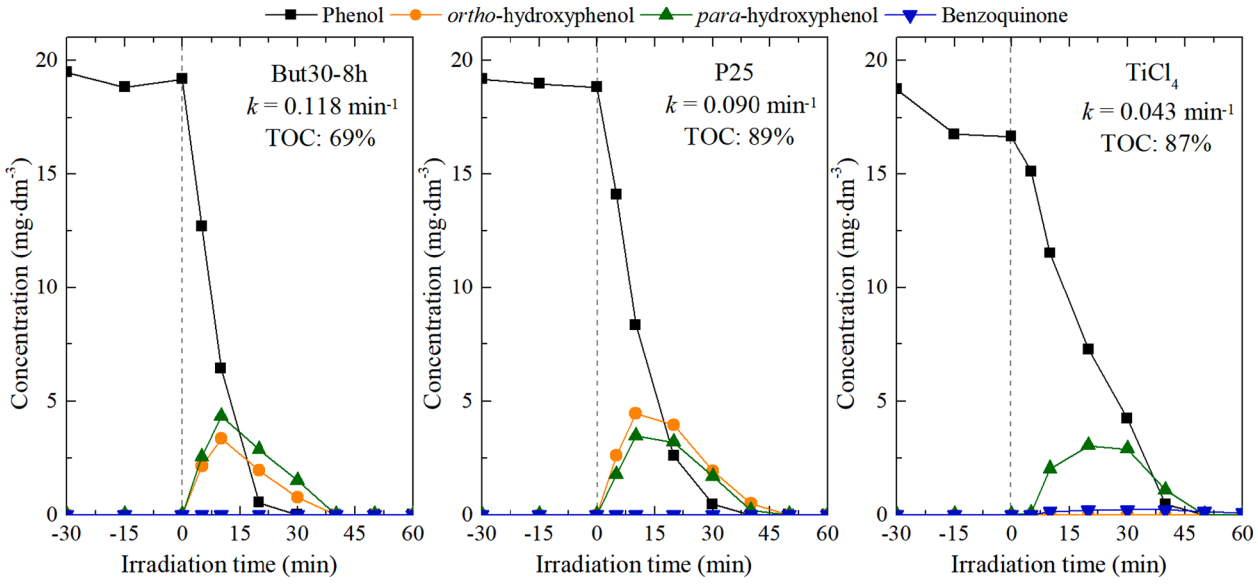

Fig. 13. A comparison of degradation and mineralization efficiency between the most active of the 2D nanoparticles, P25, and an additional control material prepared from $TiCl_4$. The preparation procedure and basic characteristics of the $TiCl_4$ sample are given in ESI.

observed enhancement of the degradation with a higher amount of surface fluorine is in agreement with the results of Mrowetz and Selli, who showed increased ˙OH generation with the fluorinated TiO_2 [79]. It could be observed as a result of F atoms influencing the surface charge distribution and raising charge separation. As presented in Fig. 14, an approximate 50% decrease of the F/Ti ratio was observed for the But30-24h sample, while Et30-24h kept its composition at a relatively constant level.

A similar reason is already well established for oxygen vacancies [80], and the different fluorine distributions/ratios between surface, subsurface, or bulk states could be a plausible explanation for some of the differences observed between samples. It could especially logically correlate with the observed differences with the synthesis environment and time (being the actual variables in the study) since the alcohol type can impact the nucleation rate of the anatase from the intermediate phase $TiOF_2$, influencing F ions distribution within the final structure.

4. Conclusions

Herein, the results of HF-assisted growth of anatase 2D nanoparticles, exposed with highly energetic {0 0 1} facets, using different alcohols as solvents were discussed in detail. The obtained results indicated that controlling both type and amount of alcohol could significantly influence the material's final properties. The morphological properties were associated with different nucleation rates, resulting from a possible ROH substitution to the $[TiF_6]^{2-}$ complex, promoting faster nucleation for short-chain alcohols through subsequent ether elimination reaction. It was found that the introduction of a low amount of n-butanol and n-hexanol can stabilize the $TiOF_2$ structure. Simultaneously, a significant increase in alcohol content promotes the formation of less platelet and less fluorinated particles due to increased H_2O produced through alcohol condensation. Moreover, the introduction of long-chain alcohols decreases TiO_2 nucleation and promotes the formation of the highly platelet nanoparticles at the early stage of the process, while ethanol and methanol produce ultrafine but more irregular-shaped particles. Compared to the control samples of commercial TiO_2 P25 and TiO_2 from $TiCl_4$ hydrolysis, the highest phenol removal efficiency was noticed for {0 0 1} nanosheets. However, the analyzed mineralization efficiency for anatase {0 0 1} facets showed lower organic carbon removal than the control sample of TiO_2 P25, which suggests their ability to break C-C bonds is relatively lower compared to other TiO_2 structures. The type of reactive species generated on the photocatalyst surface varies from different anatase structures that drive conversion to CO_2. Therefore, it can be assumed that other oxygen species are more efficient as ring-opening agents for the aromatic compounds than ˙OH radicals formed as a dominating species on the {0 0 1} facets. These results are significant regarding removing the persistent organic pollutants and studying their mineralization when discussing the surface properties of new design photocatalytic materials.

Author contributions

Anna Zielińska-Jurek: Conceptualization, Methodology, Supervision, Project administration, Writing—review and editing, Funding acquisition. **Marta Kowalkińska:** Investigation, Draft preparation. **Szymon Dudziak:** Formal analysis, Investigation, Validation, Visualization, Methodology, Draft preparation. **Jakub Karczewski:** Formal analysis. **Marcin Pisarek:** Investigation. **Adam Kubiak:** Investigation. **Katarzyna Siwińska-Ciesielczyk:** Formal analysis. **Katarzyna Siuzdak:** Formal analysis. **Anna Zielińska-Jurek:** Conceptualization, Methodology, Supervision, Project administration, Writing—review and editing, Funding acquisition. **Marta Kowalkińska:** Investigation, Draft preparation. **Szymon Dudziak:** Formal analysis, Investigation, Validation, Visualization, Methodology, Draft preparation. **Jakub Karczewski:** Formal analysis. **Marcin Pisarek:** Investigation. **Adam Kubiak:** Investigation. **Katarzyna Siwińska-Ciesielczyk:** Formal analysis.

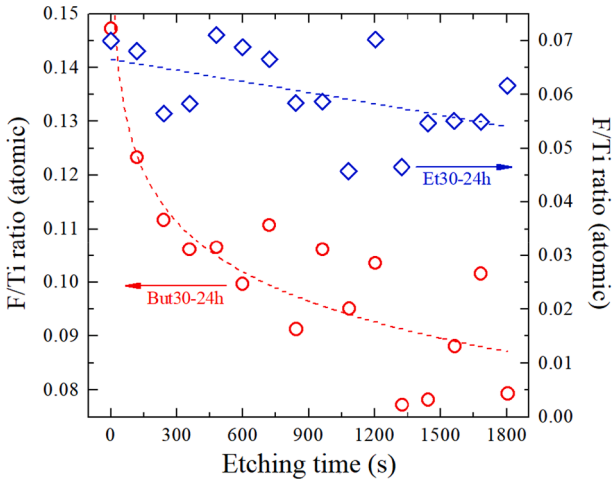

Fig. 14. The observed change in the total F/Ti ratio measured during XPS etching for samples But30-24 and Et30-24h. Presented ordinate axes have the same length.

Katarzyna Siuzdak: Formal analysis.

Funding sources

The research was financially supported by the Polish National Science Centre (grant no. NCN 2018/30/E/ST5/00845).

Declaration of Competing Interest

The authors declare that they have no known competing financial interests or personal relationships that could have appeared to influence the work reported in this paper.

Acknowledgments

The studies were carried out thanks to the Polish National Science Centre (NCN) within project no. 2018/30/E/ST5/00845. AZJ is grateful for the support of the Polish Ministry of Science and Higher Education grant no. 0525/E-359/STYP/13/2018 Scholarships for outstanding young scientists.

Appendix A. Supplementary material

Supplementary data to this article can be found online at https://doi.org/10.1016/j.apsusc.2021.150360.

References

[1] S. Ahmed, M.G. Rasul, W.N. Martens, R. Brown, M.A. Hashib, Desalination 261 (2010) 3.
[2] P.V.L. Reddy, K.H. Kim, B. Kavitha, V. Kumar, N. Raza, S. Kalagara, J. Environ. Manage. 213 (2018) 189.
[3] F. Saadati, N. Keramati, M.M. Ghazi, Crit. Rev. Environ. Sci. Technol. 46 (2016) 757.
[4] L.G. Devi, R. Kavitha, Appl. Catal. B: Environ. 140–141 (2013) 559.
[5] R. Li, X. Zhang, H. Dong, Q. Li, Z. Shuai, W. Hu, Adv. Mater. 28 (2016) 1697.
[6] S. Liu, J. Yu, M. Jaroniec, Chem. Mater. 23 (2011) 4085.
[7] H.G. Yang, C.H. Sun, S.Z. Qiao, J. Zou, G. Liu, S.C. Smith, H.M. Cheng, G.Q. Lu, Nature 453 (2008) 638.
[8] C.Z. Wen, J.Z. Zhou, H.B. Jiang, Q.H. Hu, S.Z. Qiao, H.G. Yang, Chem. Commun. 47 (2011) 4400.
[9] X. Zhao, W. Jin, J. Cai, J. Ye, Z. Li, Y. Ma, J. Xie, L. Qi, Adv. Funct. Mater. 21 (2011) 3554.
[10] Z. Wang, K. Lv, G. Wang, K. Deng, D. Tang, Appl. Catal. B: Environ. 100 (2010) 378.
[11] M.V. Sofianou, V. Psycharis, N. Boukos, T. Vaimakis, J. Yu, R. Dillert, D. Bahnemann, C. Trapalis, Appl. Catal. B: Environ. 142–143 (2013) 761.
[12] W.S. Wang, D.H. Wang, W.G. Qu, L.Q. Lu, A.W. Xu, J. Phys. Chem. C 116 (2012) 19893.

[13] N.C. Saha, F. Bhunia, A. Kaviraj, Bull. Environ. Contamination Toxicol. 63 (1999) 195.
[14] L. Zhang, T. Kanki, N. Sano, A. Toyoda, Environ. Monit. Assess. 115 (2006) 395.
[15] C.S.A. Antunes, M. Bietti, M. Salamone, N. Scione, J. Photochem. Photobiol., A 163 (2004) 453.
[16] A.M. Peiró, J.A. Ayllón, J. Peral, X. Doménech, Appl. Catal. B: Environ. 30 (2001) 359.
[17] A. Sobczyński, L. Duczmal, W. Zmudziński, J. Mol. Catal. A: Chem. 213 (2004) 225.
[18] Z. Bielan, S. Dudziak, A. Sulowska, D. Pelczarski, J. Ryl, A. Zielińska-Jurek, Materials 13 (2020) 1.
[19] T.T.T. Dang, S.T.T. Le, D. Channei, W. Khanitchaidecha, A. Nakaruk, Res. Chem. Intermed. 42 (2016) 5961.
[20] L.G. Devi, K.E. Rajashekhar, J. Mol. Catal. A: Chem. 334 (2011) 65.
[21] A. Blažková, I. Csölleová, V. Brezová, J. Photochem. Photobiol., A 113 (1998) 251.
[22] Y. Zhang, R. Selvaraj, M. Sillanpää, Y. Kim, C.W. Tai, Chem. Eng. J. 245 (2014) 117.
[23] C.H. Chiou, C.Y. Wu, R.S. Juang, Chem. Eng. J. 139 (2008) 322.
[24] A.C. Mecha, M.S. Onyango, A. Ochieng, C.J.S. Fourie, M.N.B. Momba, J. Catal. 341 (2016) 116.
[25] M. Krivec, A. Pohar, B. Likazor, G. Drazic, AIChE J. 61 (2015) 572.
[26] A.V. Emeline, X. Zhang, T. Murakami, A. Fujishima, J. Hazard. Mater. 211–212 (2012) 154.
[27] L. Suhadolnik, A. Pohar, B. Likozar, M. Čeh, Chem. Eng. J. 303 (2016) 292.
[28] X. Wang, L. Sø, R. Su, S. Wendt, P. Hald, A. Mamakhel, C. Yang, Y. Huang, B. B. Iversen, F. Besenbacher, J. Catal. 310 (2014) 100.
[29] J. Moreira, B. Serrano, A. Ortiz, H. de Lasa, Chem. Eng. Sci. 78 (2012) 186.
[30] I. Wysocka, E. Kowalska, K. Trzciński, M. Łapiński, G. Nowaczyk, A. Zielińska-Jurek, Nanomaterials (2018) 8.
[31] X. Ma, Y. Dai, M. Guo, B. Huang, Langmuir 29 (2013) 13647.
[32] S. Gao, W. Wang, Y. Ni, C. Lu, Z. Xu, J. Alloy. Compd. 647 (2015) 981.
[33] M. Kowalkińska, S. Dudziak, J. Karczewski, J. Ryl, G. Trykowski, A. Zielińska-Jurek, Chem. Eng. J. 404 (2021), 126493.
[34] H.G. Yang, G. Liu, S.Z. Qiao, C.H. Sun, Y.G. Jin, S.C. Smith, J. Zou, H.M. Cheng, G. Q. Lu, J. Am. Chem. Soc. 131 (2009) 4078.
[35] V.A. Lebedev, D.A. Kozlov, I.V. Kolesnik, A.S. Poluboyarinov, A.E. Becerikli, W. Grünert, A.V. Garshev, Appl. Catal. B: Environ. 195 (2016) 39.
[36] P. Giannozzi, et al., J. Phys.: Condens. Matter 29 (2017), 465901.
[37] P. Giannozzi, et al., J. Phys.: Condens. Matter (2009) 21.
[38] J.P. Perdew, M. Ernzerhof, K. Burke, J.P. Perdew, M. Ernzerhof, K. Burke 9982 (2010) 9982.
[39] R. Beranek, Adv. Phys. Chem. 2011 (2011) 80.
[40] Z. Huang, Z. Wang, K. Lv, Y. Zheng, K. Deng, ACS Appl. Mater. Interfaces 5 (2013) 8663.
[41] M. Li, Y. Chen, W. Li, X. Li, H. Tian, X. Wei, Z. Ren, G. Han, Small (2017) 13.
[42] T.R. Gordon, M. Cargnello, T. Paik, F. Mangolini, R.T. Weber, P. Fornasiero, C. B. Murray, J. Am. Chem. Soc. 134 (2012) 6751.
[43] J. Wang, F. Cao, Z. Bian, M.K.H. Leung, H. Li, Nanoscale 6 (2014) 897.
[44] Y. Chen, W. Li, J. Wang, Y. Gan, L. Liu, M. Ju, Appl. Catal. B: Environ. 191 (2016) 94.
[45] J. Yu, J. Fan, K. Lv, Nanoscale 2 (2010) 2144.
[46] R.O. Ragsdale, B.B. Stewart, Inorg. Chem. 2 (1963) 1002.
[47] Z. Bian, J. Zhu, H. Li, J. Photochem. Photobiol., C 28 (2016) 72.
[48] A. Vioux, Chem. Mater. 9 (1997) 2292.
[49] N. Pinna, G. Garnweitner, M. Antonietti, M. Niederberger, Adv. Mater. 16 (2004) 2196.
[50] G. Garnweitner, M. Niederberger, J. Mater. Chem. 18 (2008) 1171.
[51] R. Pazik, R. Tekoriute, S. Hakansson, R. Wiglusz, W. Strek, G. A. Seisenbaeva, Y. K. Gun'ko, and V. G. Kessler, Chem. - A Eur. J. 15 (2009) 6820.
[52] X.H. Yang, Z. Li, C. Sun, H.G. Yang, C. Li, Chem. Mater. 23 (2011) 3486.
[53] K.S.W. Sing, D.H. Everett, R.A.W. Haul, L. Mascou, R.A. Pierotti, T. Siemieniewska, Pure Appl. Chem. 57 (1985) 603.
[54] J. Liu, P. Li, Z. Sun, Z. Lu, Z. Du, H. Liang, D. Lu, Fuel 210 (2017) 446.
[56] J.Y. Ruzicka, F.A. Bakar, L. Thomsen, B.C. Cowie, C. McNicoll, T. Kemmitt, H.E. A. Brand, B. Ingham, G.G. Andersson, V.B. Golovko, RSC Adv. 4 (2014) 20649.
[57] T. Shi, Y. Duan, K. Lv, Z. Hu, Q. Li, M. Li, X. Li, Front. Chem. 6 (2018) 1.
[58] Y. Wang, L. Li, X. Huang, Q. Li, G. Li, RSC Adv. 5 (2015) 34302.
[59] Y. Wang, H. Zhang, Y. Han, P. Liu, X. Yao, H. Zhao, Chem. Commun. 47 (2011) 2829.
[60] C. Maheu, L. Cardenas, E. Puzenat, P. Afanasiev, C. Geantet, Phys. Chem. Chem. Phys. 20 (2018) 25629.
[61] N.H. Linh, T.Q. Nguyen, W.A. Diño, H. Kasai, Surf. Sci. 633 (2015) 38.
[62] J. Biedrzycki, S. Livraghi, E. Giamello, S. Agnoli, G. Granozzi, J. Phys. Chem. C 118 (2014) 8462.
[63] H. Seo, L.R. Baker, A. Hervier, J. Kim, J.L. Whitten, G.A. Somorjai, Nano Lett. 11 (2011) 751.
[64] F. Pellegrino, E. Morra, L. Mino, G. Martra, M. Chiesa, V. Maurino, J. Phys. Chem. C 124 (2020) 3141.
[65] S. Al-Hilli, M. Willander, Sensors 9 (2009) 7445.
[66] E.M. Samsudin, S.B. Abd Hamid, Appl. Surf. Sci. 391 (2017) 326.
[67] W.Q. Fang, X.L. Wang, H. Zhang, Y. Jia, Z. Huo, Z. Li, H. Zhao, H.G. Yang, X. Yao, J. Mater. Chem. A 2 (2014) 3513.
[68] X. Li, J. Yu, M. Jaroniec, Chem. Soc. Rev. 45 (2016) 2603.
[69] T. Hirakawa, K. Yawata, Y. Nosaka, Appl. Catal. A: General 325 (2007) 105.
[70] Y. Nosaka, A. Nosaka, ACS Energy Lett. 1 (2016) 356.
[71] C. Hou, W. Liu, R. Soc. Open Sci. (2018) 5.
[72] C. Adán, A. Bahamonde, M. Fernández-García, A. Martínez-Arias, Appl. Catal. B: Environ. 72 (2007) 11.
[73] J.J. Murcia, M.C. Hidalgo, J.A. Navío, J. Araña, J.M. Doña-Rodríguez, Appl. Catal. B: Environ. 179 (2015) 305.
[74] L. Mino, F. Pellegrino, S. Rades, J. Radnik, V.D. Hodoroaba, G. Spoto, V. Maurino, G. Martra, ACS Appl. Nano Mater. 1 (2018) 5355.
[75] Y. Sui, Q. Liu, T. Jiang, Y. Guo, Appl. Surf. Sci. 426 (2017) 116.
[76] R. Scotti, M. D'Arienzo, A. Testino, F. Morazzoni, Appl. Catal. B: Environ. 88 (2009) 497.
[77] A. Turki, C. Guillard, F. Dappozze, Z. Ksibi, G. Berhault, H. Kochkar, Appl. Catal. B: Environ. 163 (2015) 404.
[78] W. Yu, F. Chen, Y. Wang, L. Zhao, RSC Adv. 10 (2020) 29082.
[79] M. Mrowetz, E. Selli, Phys. Chem. Chem. Phys. 7 (2005) 1100.
[80] M. Kong, Y. Li, X. Chen, T. Tian, P. Fang, F. Zheng, X. Zhao, J. Am. Chem. Soc. 133 (2011) 16414.